

Trajectory Correction and Optimization of a Flexible Manipulator Based on a Visual Servo*

Boxi Chen¹⁾, Jiabo Feng²⁾, Xiaoke Gao¹⁾, Weijun Zhang^{#2)} and Kaihang Yu²⁾

¹⁾ Kunming Power Supply Bureau
Yunnan Power Grid Co., Ltd.
Kunming, China
199993310@qq.com

²⁾ School of Mechanical Engineering
Shanghai Jiao Tong University
Shanghai, China
xiaokegao@sjtu.edu.cn

Abstract—The tokamak in-vessel robot is a 10-DOF flexible in-vessel inspection robot designed for carrying out scanning and maintenance of a tokamak in a complicated environment. Due to the large size of the TIR, the flexible deformation of the TIR is significant, which leads to a low end positioning accuracy and trajectory accuracy. This paper analyzes the factors leading to the deformation of the TIR and establishes a model of the pose error caused by these factors. Based on the model, an error compensation method is proposed based on an optimization method. According to the principle of visual servo, the end position deviation is calculated by using the image obtained by the visual unit. The detected deviation is used to control the end position of the TIR and optimize and reduce the deviation. Experiments are carried out on a 1:1 model of a tokamak vessel, and the results show that the proposed method can effectively improve the end positioning accuracy.

Keywords—Flexible robot, End accuracy, Visual servo,

I. INTRODUCTION

The robot studied in this paper is a flexible robot designed for the inspection and maintenance of a tokamak vessel^[1], as shown in Fig. 1. According to the task requirements, several requirements are proposed to ensure that the overall inspection mission can be carried out efficiently and safely^[2].

- A safe distance between the robot and inner wall of the tokamak vessel should be maintained at all times during operation.
- High-efficiency operation should be achieved during the whole inspection process.
- To ensure the effectiveness of the image acquisition, the end of the TIR should be positioned accurately, and the pose error should be small.

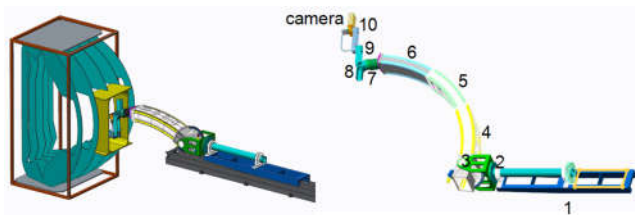


Fig. 1 Flexible in-vessel robot

The main research content of this paper is a trajectory optimization of the tokamak in-vessel robot (TIR). Based on the existing mechanical structure and software control system of the TIR, we analyze the deformation of the mechanical structure and establish an error model. First, based on the deformation of the large arm, the pose of the end of the TIR is optimized using an optimization method. Then, according to the principle of the visual servo, the end deviation is detected by image processing technology, and the end deviation is used for feedback control of the robot to improve the end positioning accuracy. Finally, a simulation and an analysis are carried out to verify the optimization method employed in the paper. Furthermore, an experiment is carried out to verify the optimization method.

II. MODEL AND PROBLEM INTRODUCTION

A. Mechanical Model

To study the motion characteristics and position error of the endoscopic TIR in the scanning process, a kinematic model of the whole endoscopic TIR must be established first. To facilitate the establishment of the model, the TIR should be considered as a whole structure connected by a series of rigid bodies through joints, as shown in Fig. 2.

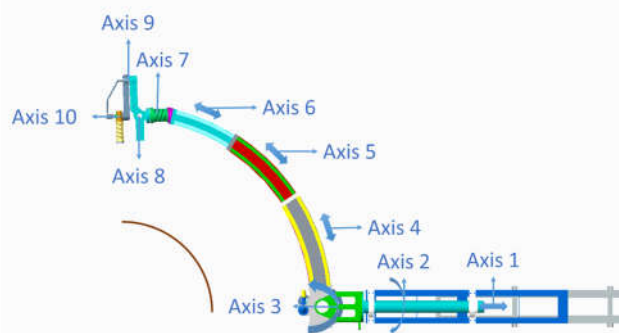


Fig. 2 The overall structure of TIR

B. Analysis for the Pose Error

(1) Posture Error of the TIR

The telescopic arm greatly expands the scanning range of the TIR, which is the key point for the TIR to expand the scanning range along the horizontal direction. However, due to the use of an aluminum alloy structure in the three telescopic arms, wear and tear of the track will occur with long-term operation. Although the wear and tear is

* This work is partially supported by China Southern Power Grid (YNKJXM20170208)

Corresponding author, zhangweijun@sjtu.edu.cn

relatively minimal, it will cause a slight deformation due to the longer extension of the arm. The wear and tear will accumulate and result in a position change that cannot be ignored at the end.

(2) Posture Error Model for the TIR

According to the analysis of Ref.[3], there are two main reasons for the deformation of the large arm: the clearance and deflection deformation. The clearance is the main reason for the end pose error. We simplify the gap deformation of the arms, as shown in Fig. 3. The arm on the right is sleeved in a sleeve on the left. Under the action of gravity, the right arm sags to form an opposite shape.

The gap between them is η . It can be found that the right arm will sag relative to the ideal position because of the gap. Therefore, the actual position relative to the ideal position is found by moving vertically downward $\eta/2$ and then rotating around the O point by the φ angle.

$$\varphi = \arcsin\left(\frac{\eta}{L}\right) \quad (1)$$

Since φ is generally a small angle, L is approximately equal to the length of the two arms overlapping each other. In fact, point O is a rotation axis in the three-dimensional space and is represented by K in the three-dimensional coordinate system. In summary, we can record K, L, η and φ as the gap parameters of the two-section arm connection.

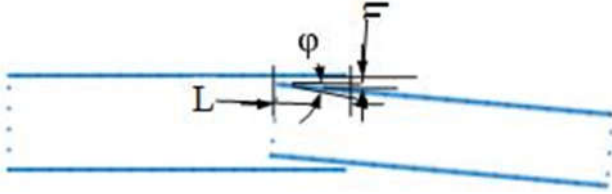


Fig. 3 The separation model between the two arms

According to the above model, one can analyze the deformation of the large arm due to the gap, as shown in Fig. 4, wherein the center of rotation is represented by K_0, K_1, K_2 . Since the large arm is an arc structure, the extension of K_0, K_1, K_2 will be placed on the axis of the large arm, and the intersection is recorded as P_1, P_2, P_3 .

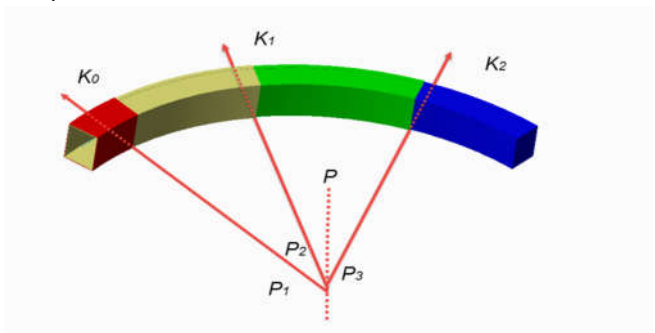


Fig. 4 The transformation analyses of the large arm

To assess the impact of the gap on the end of the large arm, we need to conduct a more in-depth analysis of the above model. First, we need to establish the coordinate system of the large arm. We take the center of the ring axis under the ideal condition of the large arm as the origin, the fan-shaped surface perpendicular to the ring axis and the center of the circle as the z-axis, and the Cartesian coordinate system with the symmetry direction of the large arm base as the x-axis, denoted as $\{A\}$. At the same time, at the end of the large arm, the center of the end of the large arm is taken as the origin, the tangential direction of the end of the axis is the x-axis, and the direction of the long side of the end matrix is the y-axis, which is denoted as $\{B\}$.

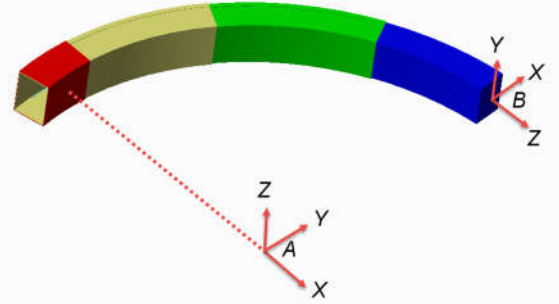


Fig. 5 The coordinate definition

Assume that the coordinate system $\{B'\}$ is the actual position of $\{B\}$ in the ideal case when the large arm is not deformed. $K_0, K_1, K_2, P_0, P_1, P_2$ can be represented as ${}^{B'}K_0, {}^{B'}K_1, {}^{B'}K_2, {}^{B'}P_0, {}^{B'}P_1, {}^{B'}P_2$ in the $\{B'\}$ coordinate system. $\text{Rot}(K, P, \varphi)$ is written as an arithmetic operator φ that takes a straight line passing through the K direction and passing through P .

(2-31)

$${}^{B'}T = \text{Rot}({}^{B'}K_3, {}^{B'}P_3, \varphi_3) \text{Rot}({}^{B'}K_2, {}^{B'}P_2, \varphi_2) \cdot \text{Rot}({}^{B'}K_1, {}^{B'}P_1, \varphi_1) \quad (2)$$

$$\begin{aligned} {}^AT &= {}^AT {}^{B'}T = {}^AT \cdot \text{Rot}({}^{B'}K_3, {}^{B'}P_3, \varphi_3) \\ &\cdot \text{Rot}({}^{B'}K_2, {}^{B'}P_2, \varphi_2) \text{Rot}({}^{B'}K_1, {}^{B'}P_1, \varphi_1) \\ &= {}^AT \cdot \text{Rot}({}^{B'}T {}^AK_3, {}^{B'}T {}^AP_3, \varphi_3) \\ &\cdot \text{Rot}({}^{B'}T {}^AK_2, {}^{B'}T {}^AP_2, \varphi_2) \text{Rot}({}^{B'}T {}^AK_1, {}^{B'}T {}^AP_1, \varphi_1) \end{aligned} \quad (3)$$

To solve the problem $\text{Rot}(K, P, \varphi)$, the problem can be described in terms of the coordinate systems $\{M\}$ and $\{N\}$, which initially coincide with each other. We rotate $\{N\}$ around the vector K through point P with an angle of rotation of φ . Then, we find a description of the coordinate system $\{N\}$.

For the convenience of the latter description, let us record

$$\begin{cases} K = {}^M K = [k_x \ k_y \ k_z]^T \\ P = {}^M P = [p_x \ p_y \ p_z]^T \end{cases} \quad (4)$$

The tag defines two new coordinate systems $\{M'\}$ and $\{N'\}$ at the same time. Their origins coincide with each other, and the coordinate systems have the same direction relative to the coordinate systems $\{M\}$ and $\{N\}$, but their origins are on the axis of rotation. We choose

$${}^M_{M'}T = \begin{bmatrix} 1 & 0 & 0 & p_x \\ 0 & 1 & 0 & p_y \\ 0 & 0 & 1 & p_z \\ 0 & 0 & 0 & 1 \end{bmatrix} \quad (5)$$

Similarly, the description of the coordinate system $\{N'\}$ relative to $\{N'\}$ is

$${}^N_{N'}T = \begin{bmatrix} 1 & 0 & 0 & -p_x \\ 0 & 1 & 0 & -p_y \\ 0 & 0 & 1 & -p_z \\ 0 & 0 & 0 & 1 \end{bmatrix} \quad (6)$$

The coordinate system $\{N'\}$ is obtained by rotating $\{M'\}$ around the origin vector, which can be directly applied to the equivalent rotation matrix around the general rotation axis.

$${}^N_{M'}T = \begin{bmatrix} k_x k_x v\varphi + c\varphi & k_x k_y v\varphi - k_z s\varphi & k_x k_z v\varphi + k_y s\varphi & 0 \\ k_x k_y v\varphi + k_z s\varphi & k_y k_y v\varphi + c\varphi & k_y k_z v\varphi - k_x s\varphi & 0 \\ k_x k_z v\varphi - k_y s\varphi & k_y k_z v\varphi + k_x s\varphi & k_z k_z v\varphi + c\varphi & 0 \\ 0 & 0 & 0 & 1 \end{bmatrix} \quad (7)$$

With $c\varphi = \cos \varphi$, $s\varphi = \sin \varphi$, $v\varphi = 1 - \cos \varphi$, finally, the transformation equation can be obtained.

$${}^M_N T = {}^M_{M'} T {}^{M'}_{N'} T {}^N_{N'} T \quad (8)$$

When the gap is $\eta = 4$ mm, the position of the end deformation is as shown in Figs. 2-5. During the unfolding of the large arm, the end will gradually sag. When the large arm is fully deployed, the displacement of the end relative to the ideal position will reach 56 mm.

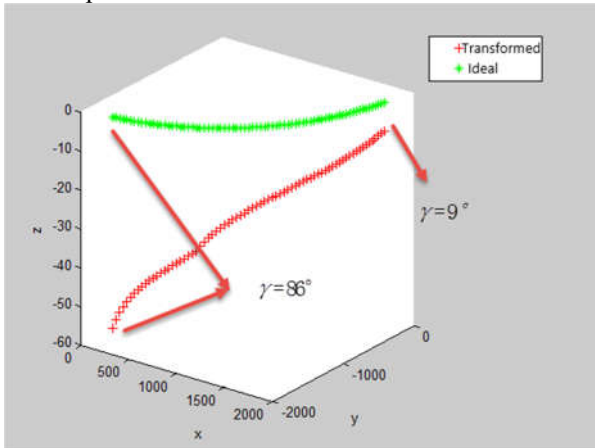


Fig. 6 Comparison of the transformed and ideal

(3) Experimental results

According to the previous analysis, the horizontal tester is placed at the initial end and the end of each arm; in

addition, according to the rules of the cavity entry, after the completion of the movement of the cavity, the moving base remains motionless, which mainly plays a supporting role. Then, the first arm is extended, and the second arm is extended after the first arm is fully extended. After the second arm is fully extended, the third arm is extended until it is fully extended. The tilt angle of the arm relative to the horizontal line is measured.

Then, when the arm is fully deployed, the sag of the whole arm is measured with a high-precision level instrument at the initial level, as shown in Fig. 7.

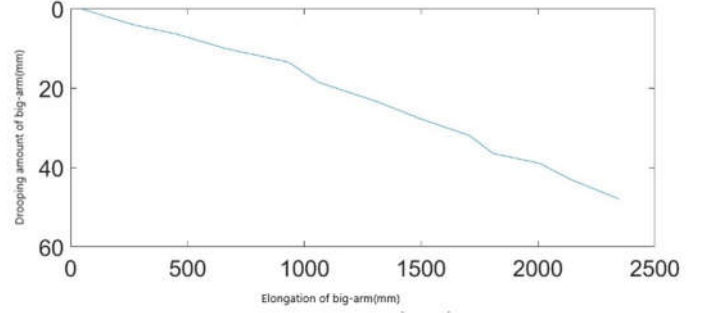


Fig. 7 Change in the deformation of the large arm

According to Fig. 7, the amount of deformation of the large arm gradually increases during the continuous development of the large arm, and η can reach 50 mm when the large arm is fully deployed. At this time, γ reaches a maximum of 2° . This verifies our analysis of the deformation of the large arm.

III. END EFFECTOR

A. Modified Achievability Analysis

After establishing the error model in Section 2, we found that the ends of the large arm have offsets in the x, y, z directions. Since the error in the y direction is the largest, the deviation in the y direction is considered first. First, the large arm is simplified as a single-ended fixed cylinder. When the leftmost level is horizontal, the simplified model of the large arm is shown in Fig. 8.

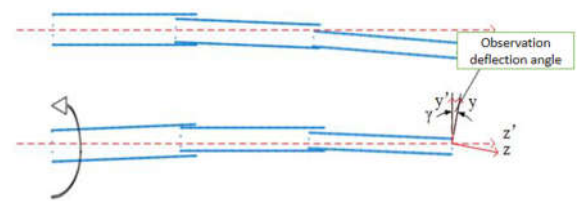


Fig. 8 Model of the deformation of the large arm and initial adjustment

Subsequent preliminary adjustments are made. First, we raise the large arm by moving the rotating joint of the base, change the position of the large arm, and make a preliminary adjustment to the large arm so that η is equal to 0. Then,

$${}^o_o T = T_z(\alpha) T_x(\gamma) \quad (9)$$

The position deviation caused by the z-axis can be compensated directly by adjusting the first section a_{07} of the forearm, but a single robot arm cannot fully compensate for the rotation deviation of the x-axis direction; however, the second section of the forearm can achieve a partial compensation, which is the focus of this section. Rotate the left end of the large arm to adjust the end of the large arm so that it is the same level as the left end. In the ideal case, the end coordinate system is represented by $x'y'z'o'$. In the actual case, the end coordinate system is $XYZO$, and $XYZO$ is obtained by rotating $x'y'z'o'$ in the negative direction about the x-axis. The representation of $XYZO$ in $x'y'z'o'$ can be expressed by a formula.

After the initial adjustment, although the end position is already at the target horizontal line, the deformation still affects the camera observation, which is formed as an observation declination in the direction perpendicular to the scanning section, as shown in the second figure of Fig. 8.. To obtain better observations, we analyze them next.

B. Trajectory Optimization Algorithm Based on an Error Analysis

Let the original design track be

$$\theta_1 = q_1(t), \theta_2 = 0, \theta_3 = q_3(t), \theta_4 = q_4(t) \quad (10)$$

Ideally, the terminal posture is represented by a matrix:

$$T_1 = {}^0_5T \Big|_{\theta_1=q_1(t), \theta_2=0, \theta_3=q_3(t), \theta_4=q_4(t)} \quad (11)$$

Let the modified trajectory be

$$\theta_1 = \hat{q}_1(t), \theta_2 = \hat{q}_2(t), \theta_3 = \hat{q}_3(t), \theta_4 = \hat{q}_4(t) \quad (12)$$

The actual pose matrix can be expressed as

$$T_s = {}^0_5T \Big|_{\theta_1=\hat{q}_1(t), \theta_2=\hat{q}_2(t), \theta_3=\hat{q}_3(t), \theta_4=\hat{q}_4(t)} \quad (13)$$

Subtracting equation (13) from equation (11), we have

$$\Delta T = \begin{bmatrix} \Delta R & \Delta P \\ 0 & 0 \end{bmatrix} = T_1 - T_s \quad (14)$$

where A is the pose deviation matrix, defined as

$$\begin{cases} \hat{q}_1(t) = q_1(t) \\ \hat{q}_3(t) = q_3(t) \\ \hat{q}_4(t) = q_4(t) \end{cases} \quad (15)$$

For any moment t_1 , θ_1 , θ_2 , θ_3 is known so that the function ΔT , ΔR , ΔP about θ_2 can be obtained. To obtain the correction, θ_2 can be obtained to minimize the norm of ΔT . When calculating θ_2 , the speed and acceleration should be limited to a certain range to ensure the smoothness of the joint motion.

To find the best θ_2 , we employ a one-dimensional search, with $\theta_2 = 0$ as the initial point, let the norm of ΔT be $f(\theta_2)$, and determine a search direction $d^{(k)}$ according

to some rules, starting from $\theta_2^{(k)}$ and moving along the search direction $d^{(k)}$. The minimum point of the norm of ΔT is found on the straight line, resulting in a subsequent point $\theta_2^{(k+1)}$ of $\theta_2^{(k)}$. We repeat the above steps until we obtain the best θ_2 .

IV. OPTIMIZATION BASED ON VISUAL FEEDBACK

A. Grayscale Processing

In the scanning process, the image detected by the end camera is an unprocessed image. Before image processing, RGB images need to be transformed into gray images. The formulas are as follows:

$$GREY = REY \times 0.299 + GREEN \times 0.587 + BLUE \times 0.114 \quad (16)$$

B. Binarization and Skeleton Extraction

Due to the complex and variable working environment of the TIR, such as the uneven illumination, the difference between the image target feature and the background pixel after graying is relatively small. In this case, the global threshold method is no longer applicable.. To avoid features being ignored, a local threshold selection method is required in relatively complicated situations.

It can be seen from Fig. 9 that the binarized image obtained by the local threshold method is more effective in filtering more suitable pixels than the binarized image obtained by the global threshold method; however, because the gap is large, the selected area is quite complicated. The skeleton needs to be extracted, which is essentially a process of "refining" the image.

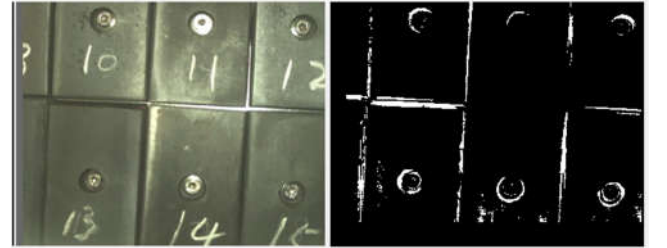


Fig. 9 Rendering of the local threshold

This paper uses the skeleton extraction method based on Zhang. First, each pixel and its neighborhood are divided as follows:

P9 (i-1,j-1)	P2 (i-1,j)	P3 (i-1,j+1)
P8 (i,j-1)	P1 (i,j)	P4 (i,j+1)
P7 (i+1,j-1)	P6 (i+1,j)	P5 (i+1,j+1)

Fig. 10. Pixel point and its neighborhood division

As shown in Fig. 10, by examining the P1 point to determine whether to retain the P1 point, we first traverse the gray levels of each neighborhood in the order of P2, P3, P4... P8, and P9; the frequency 0 is converted to 1 and represented as A(P1), the number of nonzero pixel points is

represented as $B(P1)$, and if $P1$ point satisfies the following four conditions at the same time, it is deleted.

$$2 \leq B(P1) \leq 6 \quad (17)$$

$$A(P1) = 1 \quad (18)$$

$$\begin{cases} P2 \times P4 \times P6 = 0 \\ P2 \times P4 \times P8 = 0 \end{cases} \quad (19)$$

$$\begin{cases} P4 \times P6 \times P8 = 0 \\ P2 \times P6 \times P8 = 0 \end{cases} \quad (20)$$

With the above method, each pixel is screened until all the points meet the condition, and then image extracted by the skeleton based on Zhang is obtained as shown in Fig. 11.

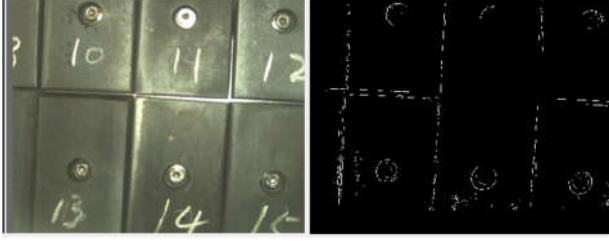


Fig. 11 Rendering of the skeleton extraction

C. Edge Detection

Solitary and nonvertical points can be removed by a Sobel horizontal operator calculation^[6], as shown in Fig. 12.2.



Fig. 12 Rendering of the Sobel operator

D. Feature Extraction

After the edge detection and binarization are carried out, a binary image with edges is obtained. At this time, the geometric features and other target features in the image can be recognized by the algorithm.

Several straight lines are detected in the area of each gap. For this reason, we aggregate the stronger lines into the same straight line by employing a horizontal midline intercept, as shown in Fig. 13.

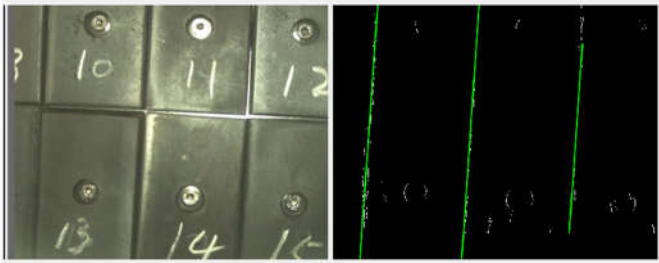


Fig. 13 Linear polymer

At this point, we have obtained a straight line that meets the requirements in all fields of view. Selecting the line near the middle of the field of view is our target line. However, during the movement of the arm, the centerline will have an

offset. To prevent the two different gaps from being mistaken as a gap during the movement, we employ a straight line in the center of the field of view to calculate the distance from the target line in real time. It is limited to the same gap between the target line and the vertical centerline in the two frames before and after the screen is less than 1/3 of the screen. As shown in Fig. 14, the observed declination in the field of view can be obtained according to the k, b parameter of the acquired line.

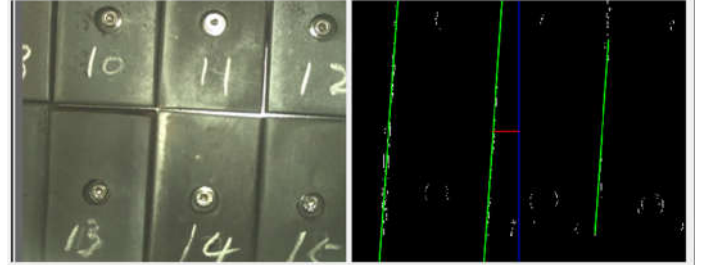


Fig. 14 Target line tracking

E. Design of the Visual Servo Controller

After the image processing, the visual servo controller can effectively acquire the features of the target in the image. According to the calculation of the tilt angle between the end of the real-time output TIR and the vertical direction, an optimal algorithm is used to calculate the joint that should be adjusted by the second joint of the forearm under the current visual deflection angle. Then, according to the relationship for the conversion between the joint space and actuator space, the motion parameters that should be sent to the lower computer are calculated so that the motion of the TIR can be adjusted in real time according to the visual image.

V. SIMULATION AND EXPERIMENT

A. Simulation

To verify the effect of our trajectory optimization algorithm, we used the Robotics Toolbox to perform simulation experiments on forward and backward kinematics, trajectory planning, and dynamics and to carry out a positive kinematics calculation of the TIR to obtain the end trajectory. A comparison with the trajectory under ideal conditions is shown in Fig. 15.

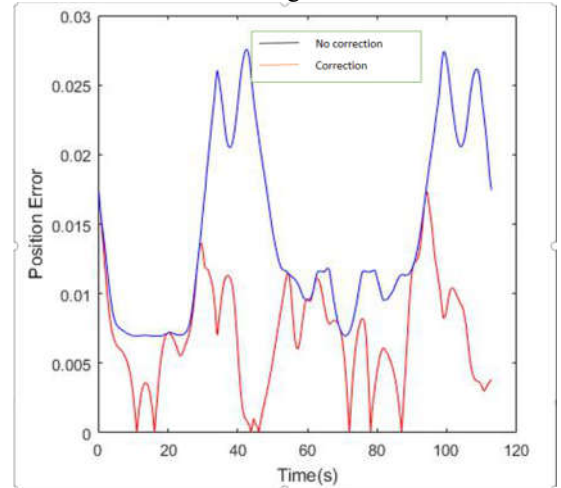


Fig. 15 End effector trajectory optimization

According to the calculation results, we find that after the trajectory optimization algorithm, both of them have greatly optimized the error of the TIR, and the correction effect is consistent with the theory.

B. Motion experiment based on the modified algorithm

For the algorithm designed previously, we employ the motion platform of the automatic scanning experiment as the experimental platform. In this experiment, we aim to verify the effectiveness of the optimization algorithm based on the visual servo.

As shown in Fig. 16, during the scanning process, the image captured by the optimization algorithm is compared with the image captured by an algorithm without optimization.

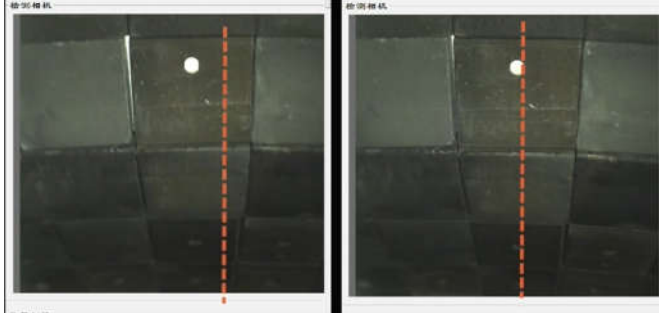


Fig. 16 Comparison of the visual images

According to the obtained images, it can be seen that the motion trajectory of the end of the TIR has been greatly improved and the pose error of the end has been reduced by using the visual servo optimization algorithm.

CONCLUSION

In this paper, we mainly study a method to improve the end effector positioning accuracy of the TIR. The cause of the deformation of a flexible mechanism is analyzed, and an error model is established. According to the error model, this paper uses an optimization method to modify the trajectory of the end effector and improve the end effector accuracy. The image obtained by the end effector is used to determine the pose error by image processing technology. According to visual servo theory and the error model, the terminal position is adjusted to reduce the positioning error.

REFERENCES

- [1]. J. Peng X, Yuan J, Zhang W, et al. Kinematic and dynamic analysis of a serial-link robot for inspection process in EAST vacuum vessel[J]. Fusion Engineering and Design, 2012, 87(5): 905-909.
- [2]. J. Gargiulo L, Bayetti P, Bruno V, et al. "Operation of an ITER relevant inspection robot on Tore Supra Tokamak". Fusion Engineering and Design, 2009, 84(2): 220-223.
- [3]. C. Dongmei X, Daokui Q, Fang X. "Path constrained time-optimal robot control". Proceedings of The International Conference on Robotics and Biomimetics, 2006: 1095-1100
- [4]. M. Gasparetto A, Boscariol P, Lanzutti A, et al. "Path Planning and Trajectory Planning Algorithms: A General Overview". Motion and Operation Planning of Robotic Systems. Springer International Publishing, 2015: 3-27.
- [5]. Zhao Qingjie, Lian Guangyu, Sun Zengqi. "Survey of Robot Visual Servoing". Control and Decision, 2001, 16(6): 849-953.
- [6]. Zhang Jingxi, Cao Qi, Zuo Pan, Zhang Wenlong, Tang Wei, Li Xinke. "Series mechanical arm and visual control". Electronic Test, 2017(09): 32-33.